Electrical Imaging and 3D Modeling of a Discontinuous Aquifer: Insights from Toumbakro, Bouaké, Côte d'Ivoire

Kouamé Gbèlè Hermann Loukou[1], Loukou Nicolas Kouamé[2],
Kouao Laurent Kouadio[3]

[1] *Université de Man, Unité de Formation et de Recherche des Sciences Géologiques et Minières, Man, Côte d'Ivoire,*
e-mail: loukou90@yahoo.fr (corresponding author), ORCID ID: 0009-0001-0999-799X
[2] *Université Félix Houphouët-Boigny, Unité de Formation et de Recherche des Sciences de la Terre et des Ressources Minières,*
Abidjan, Côte d'Ivoire, e-mail: moayek@gmail.com
[3] *Central South University, School of Geosciences and Info-physics, Changsha, China, e-mail: lkouao@csu.edu.cn,*
ORCID ID: 0000-0001-7259-7254

Abstract: A geophysical survey using electrical imaging in the Wenner–Schlumberger configuration was carried out in a crystalline basement region in central Côte d'Ivoire to improve knowledge of the aquifers in this area affected by recurrent water stress. The 2D resistivity sections, corroborated by petrographic field observations and drilling data, led to the development a 3D conceptual model of the aquifers in the study area. This model distinguishes three main lithological units: a resistant surface cover consisting of a lateritic cuirass, a conductive alteritic layer, and, at the base, a more or less fractured crystalline basement. From a structural point of view, several fracture networks have been identified, with predominantly NW–SE, NNW–SSE, and N–S orientations, constituting potential groundwater circulation zones.

Keywords: electrical imaging, aquifer, 3D conceptual model, Cote d'Ivoire

INTRODUCTION

In West Africa, the basement occupies more than 80% of the territory (MacDonald & Davies 2000) and is generally composed of hard, non-porous, impermeable rocks. However, these rocks undergo physical and chemical modifications under weathering and tectonics, giving them hydrodynamic properties such as fracture permeability. Consequently, these hard rocks' altered and fractured parts constitute discontinuous aquifers representing the population's primary water supply source (Taylor et al. 2009, Dewandel et al. 2010, Soro 2017). Unlike surface water, these aquifers are perennial water resources less vulnerable to climatic pressures and pollution. However, access to these groundwater resources, commonly provided by boreholes, is not always straightforward. Indeed, many boreholes, especially in complex hydrogeological zones, generally fail. This is the case especially in the Bouaké department, where out of a sample of 162 boreholes drilled in the 1980s, only 28 provided a high flow rate ($Q \geq 5$ m³/h), capable of justifying an urban water supply system,

i.e., a failure rate of ca. 83% (Loukou et al. 2022). Consequently, it reveals the complexity of aquifers in basement zones and the need to develop conceptual models specific to each hydrogeological context.

Therefore, this work aims to improve knowledge of the Bouaké aquifers through local-scale geoelectric characterization at a selected site.

OVERVIEW OF THE TOUMBAKRO SITE

Geographical context

Toumbakro site, covering an area of 100 ha, is located in central Côte d'Ivoire, more precisely in the northern part of the Bouaké department, around 372 km north of Abidjan, in the Gbêkê region, at 287,000 m longitude and 873,000 m latitude (Fig. 1). The Baoule-type climate is marked by two main seasons: a relatively severe dry season from November to February, characterized by the harmattan (a cool, dry wind that blows from December to February), and a rainy season from March to June. In addition, there are two short seasons: a short dry season starting in July and ending in August, and a short rainy season starting in September and ending in October.

Overall, average annual rainfall varies between 1,200 mm and 1,600 mm (Kouassi et al. 2008). Temperatures fluctuate between 25°C and 38°C (Assemian et al. 2023).

Geological context

Lateritic cuirasses cover the Toumbakro site. Some are in the form of slabs (Fig. 2A), while others are in the form of scattered blocks (Fig. 2B).

The weathering profile thus consists, at the top, of an upper, reddish ferruginous slab. The armor-plated horizon covers almost the entire site. This surface level is rugged and compact but also has cavities and fracture zones through which water infiltrates to regain the underlying horizon. According to borehole logs in the area, the bedrock is granitic.
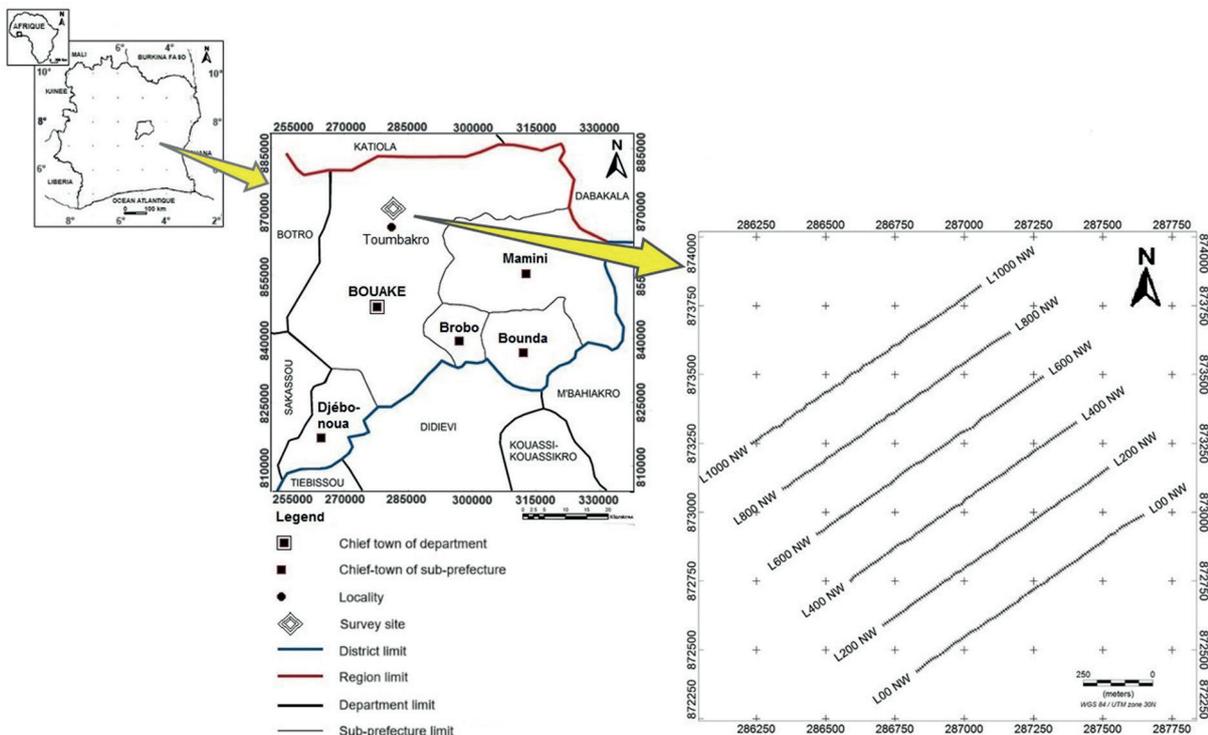

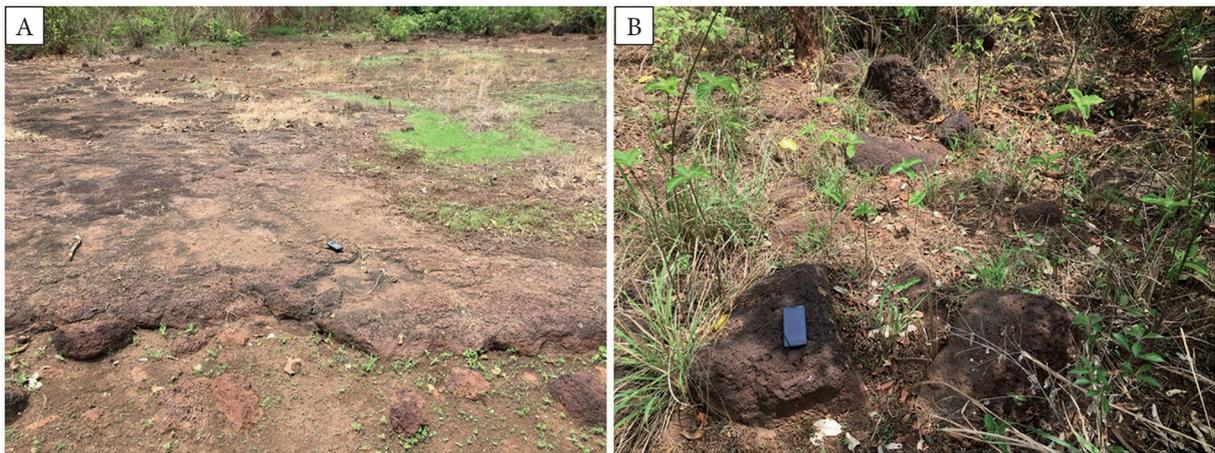***Fig. 1.*** *Location of the Toumbakro site*

Fig. 2. *Lateritic cuirasse at Toumbakro: A) in slab form; B) in blocks*

DATA

The technique used for data acquisition, electrical imaging, provides resistivity values of the subsurface, both laterally and vertically, offering a precise visualization of geological structures. Measurements are carried out using a Syscal Pro Switch 72 resistivity meter in a Wenner–Schlumberger configuration, renowned for its ability to detect horizontal and vertical subsurface structures while minimizing interference from ambient noise.

For this study, six parallel resistivity profiles were acquired during the survey with a line spacing of 200 m, each with a length of 1,070 m, oriented along an azimuth of N55°. A spacing of 10 m between electrodes is chosen to guarantee the optimum resolution at both surface and depth. The quality of the acquired data is carefully controlled, particularly by correcting anomalies linked to measurement errors or electronic contact conditions, to ensure maximum reliability during data processing and inversion.

METHOD

Electrical imaging is a non-invasive technique for obtaining the distribution of subsurface electrolytic resistivity in both the horizontal and vertical planes. This study applied this method using the Wenner–Schlumberger configuration, which

is renowned for detecting horizontal and vertical structures while remaining relatively insensitive to noise interference. This hybrid configuration combines the advantages of the Wenner (stability against noise) and Schlumberger (increased sensitivity to resistivity variations with depth) configurations.

Measurements were carried out using a Syscal Pro Switch 72 resistivity meter from Iris Instruments, a device commonly used for resistivity surveys due to its accuracy and robustness.

During the survey, the acquisition parameters were set uniformly across all measurements. The current injection pulse duration was fixed at 0.5 seconds. The adopted standard deviation threshold was $Q = 0$. The number of measurement cycles varied between three and five, with three cycles used when $Q < 0$ and five cycles when $Q > 0$. Finally, the injection voltage applied during the measurements was 400 V.

Data processing and inversion

The raw data obtained underwent recurrent digital inversion to visualize the subsurface geological formations. The inversion utilized the Gauss–Newton regularization algorithm (Günther 2004), executed within Res2DINV software. This software is extensively utilized in electrical resistivity imaging, particularly for its efficacy in inverting complex data on heterogeneous layers. The approach relies on Equation (1), which reduces

discrepancies between observed data and the generated resistivity model at each iteration:

$$\left(S^T D^T D S + \lambda C^T C\right) \cdot m_k =$$
$$= S^T D^T D(d - f(m_k)) - \lambda C^T C(m_k - m_0) \tag{1}$$

with:

$$C^T C = \alpha_x C_x^T C_x + \alpha_y C_y^T C_y + \alpha_z C_z^T C_z \,,$$

where: m_0 – reference model; m_k – model at iteration k; S – sensitivity matrix; λ – regularization factor; D – data weighting matrix; C – stress matrix; d – vector of apparent resistivity data containing N values; $f(m_k)$ – direct modeling response m at iteration k; α_x, α_y, α_z – anisotropic weights applied in each spatial direction (x, y, z).

Equation (1) also considers the possibility of applying anisotropic regularization, where each direction can be weighted differently according to the importance attributed to the variability of the structures.

Calculating the error

At each iteration, the difference between the calculated apparent resistivities ($x_{\text{model},i}$) and the measured apparent resistivities ($x_{\text{data},i}$) is evaluated using the RMS (root mean square), an error indicator defined by Equation (2):

$$RMS = \sqrt{\frac{\sum\limits_{i=1}^{N} \left(\frac{\left(x_{\text{data},i} - x_{\text{model},i}\right)^2}{x_{\text{data},i}} \right)}{N}} \tag{2}$$

where: $x_{\text{data},i}$ – the apparent resistivity measured for the i-th data; $x_{\text{model},i}$ – the apparent resistivity calculated for the i-th data; N – the total number of measurements performed.

This method makes it possible to progressively adjust the numerical model to converge towards an optimal solution, with minimal residual error, while respecting the physical and geological constraints of the layer.

3D modeling

After inversion, the interpretation of the 2D resistivity sections not only made it possible to identify the main geoelectrical units of the subsurface but also to reveal the presence of discontinuous structures interpreted as fractures. The delineation of these features was carried out by identifying discontinuities affecting the geological formations, characterized by relatively low resistivity contrasts associated with fractured zones.

In addition to the 2D inversions, a 3D conceptual model was built from the resistivity sections obtained and field observations. This model was developed using Surpac software, which integrates geophysical and geological data to generate 3D representations of the subsurface. This innovative model type enables finer visualization and interpretation of complex structures, including fracture networks and groundwater accumulation zones.

RESULTS

Interpretation of 2D resistivity sections

The 2D resistivity sections provide a detailed depiction of the subsurface structure and its lateral variations. These results enable the identification of the main geoelectric units and the delineation of potentially aquifer-bearing zones.

Profile L00

Figure 3 shows the 2D resistivity section of profile L00, which distinguishes three layers. At the top is a resistant surface layer R1, with a wall depth of no more than 20 m. This layer has an irregular thickness along the profile. Based on lithological observations in the field, R1-resistant geological unit corresponds to the cuirass.

Beneath the R1 layer lies a conductive layer C with resistivity values 20–630 $\Omega \cdot$m. It corresponds to the alterite aquifer, through which meteoric water infiltrates. This infiltration is facilitated by the absence of the R1 layer between stations 0 and 130 and by the fractured R1 layer between stations 130 and 700.

The R1-C unit, interpreted as an alteration profile, rests on an even more resistant geological unit, R2, which corresponds to the basement. This resistant R2 bedrock peaks at around 20 m depth at the extreme southwest of the profile. The depth of its roof gradually increases towards the central part until it reaches a depth more significant than the depth of investigation, causing the basement to disappear. It then reappears at station 800 and gradually rises towards the northeast to a depth of 30 m.
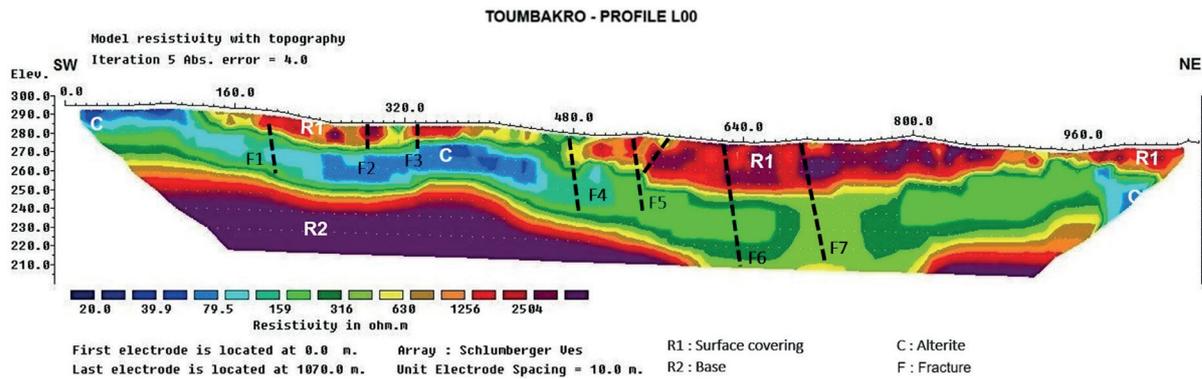
Fig. 3. *2D resistivity section of profile L00*

However, between stations 690 and 740, the resistant R2 layer is not visible. This absence is linked to the subsidence of the basement roof, observed between stations 600 and 800, due to the presence of the F7 fracture. It has contributed to lowering resistivity values in this area, which is likely to be a suitable zone for drilling as it may potentially contain water.

Profile L200 NW

At the top, the L200 NW profile reveals a lateritic cuirass materialized by a superficial resistant zone (R1) with a maximum thickness of ca. 20 m, absent between stations 0 and 130. This surface cover (R1) overlies a conductive zone (C), corresponding to the alterite layer, which constitutes a potential accumulation zone for surface water (Fig. 4).

At the base, an even more resistant bedrock (R2) is identified, with a topography similar to that previously observed on profile L00. However,

a more marked continuity of the two R2 components, located respectively to the southwest and northeast of the profile, is visible. This continuity suggests a progressive deepening of the sound basement roof from southwest to northeast.

Profile L400 NW

Section L400 NW shows a structure comprising three geoelectric units (Fig. 5). From top to bottom, they are:
- a resistant surface covering R1 (630–3,233 $\Omega \cdot$ m) corresponding to the cuirass;
- a conductive layer C (20–630 $\Omega \cdot$m) corresponding to the alterite;
- a more resistant bedrock R2, subdivided into two sub-units, namely the fractured bedrock represented by a thin layer of intermediate resistivities between 630 $\Omega \cdot$ m and 1,800 $\Omega \cdot$m and by the sound bedrock at the base with resistivities above 1,800 $\Omega \cdot$m.
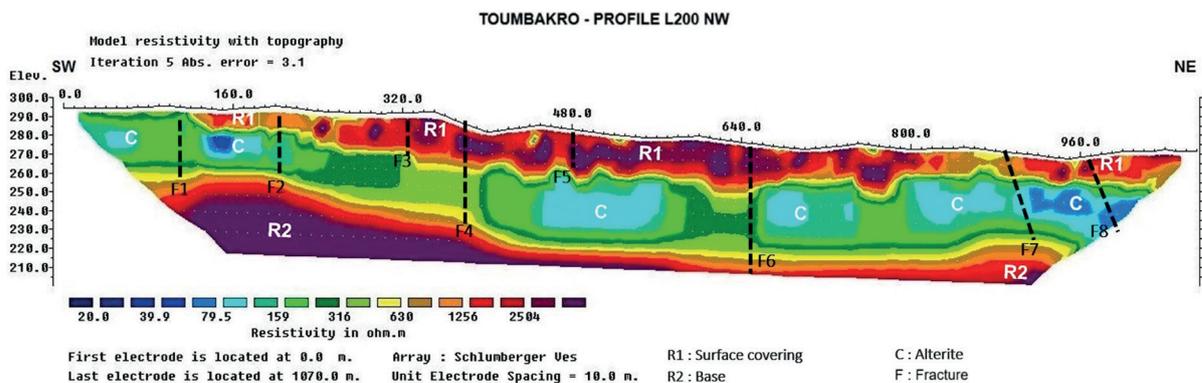

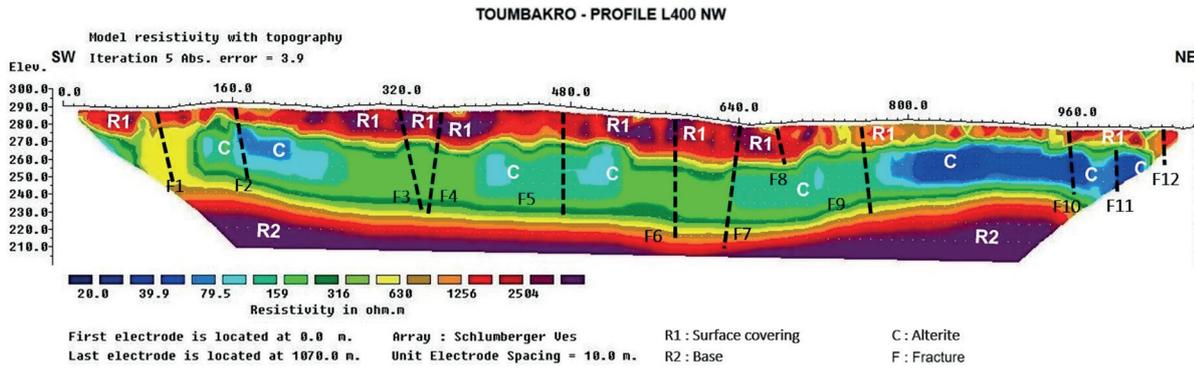**Fig. 4.** *2D resistivity section of the L200 NW profile*

Fig. 5. *2D resistivity section of profile L400 NW*

In the same order of depth as profiles L00 and L200 NW, the roof of the R2 resistant layer is perceptible at 40 m at the southwest and northeast ends of the profile and 60 m in the central part. In addition, numerous fractures mark the 2D section of profile L400 NW, two of which are located in the center of the profile and would have contributed to the subsidence of the basement roof.

Profile L600 NW

Three layers are visible on the L600 NW profile (Fig. 6). The first few meters of depth are occupied by an R1-resistant layer (630–3,233 $\Omega \cdot m$). It extends along the entire profile length, with thickness and resistivity gradually decreasing from southwest to northeast. In addition, numerous vertical discontinuity ties dissect the resistant R1 layer, which correspond to fractures that could serve as drains for groundwater recharge. From a hydrogeological point of view, these are rainwater infiltration zones. It explains the underlying ground's low resistivity (20–630 $\Omega \cdot m$). In fact, just below the R1 layer lies a much more pronounced conductive C complex to the northeast of the profile. The R1-C complex is affected by numerous break-like discontinuities. Conductive layer C results from an accumulation of water that probably constitutes an aquifer. Unit C, which corresponds to an aquifer, rests on a more resistant R2 layer.

Profile L800 NW

On profile L800 NW, the subsoil comprises three geoelectric units: a resistant surface cover R1, a conductive ground C, and a very resistant bedrock R2 (Fig. 7). As shown in the L600 NW profile, the R1 surface overburden has a high resistivity (630–3,233 $\Omega \cdot m$) and a thickness of around 10 m, which gradually decreases from SW to NE.
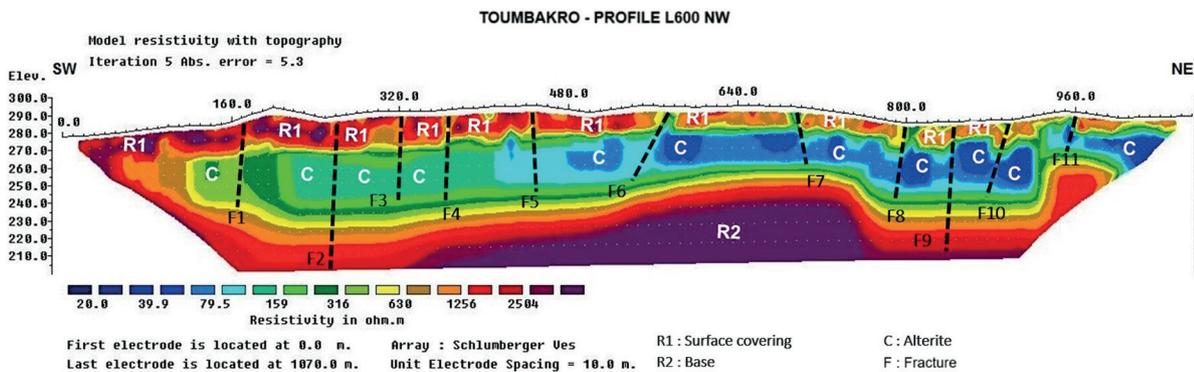

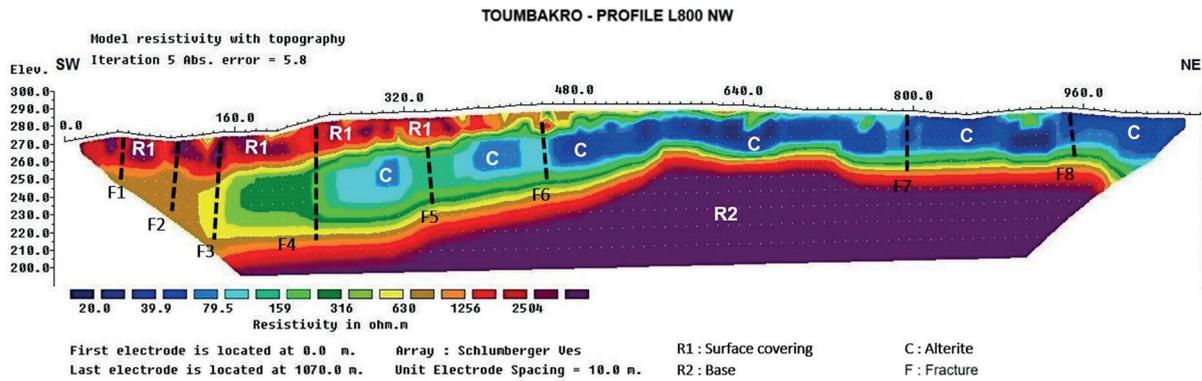**Fig. 6.** *2D resistivity section of profile L600 NW*

Fig. 7. *2D resistivity section of profile L800 NW*

This overburden disappears from station 500 onwards, exposing conductive layer C at the surface in the northeast section, more precisely between stations 500 and 1070. Layer C corresponds to a groundwater accumulation zone. The thickness of layer C reaches 40 m to the southwest and is around 20 m on the northeast side of the profile. The resistant R2 bedrock, with its much higher resistivity, has a significantly shallower roof (20–40 m) than the previous profiles.

Profile L1000 NW

Section L1000 NW reveals the existence of three geoelectric units: aresistant surface cover (R1), a conductive ground (C), and a resistant bedrock (R2) (Fig. 8). The thickness and resistivity of the R1 soil also decreases from southwest to northeast

and tends to disappear in the central part of the profile, more precisely at station 480. Field observations indicate that the resistive R1 corresponds to the cuirass.

The R1-C complex rests on the resistant R2 bedrock. As in the previous profile, the R2 bedrock not only peaks at a shallower depth (20 m), but also appears to be particularly affected by F8 and F9 fractures between stations 480 and 960. Indeed, at stations 260 and 710, zones of relatively low resistivity (around 1,300 $\Omega \cdot m$) stand out with the immediate environment, clearly separating the resistant domain (around 3,000 $\Omega \cdot m$) into three compartments. These openings correspond to fractures F8 and F9, which create a depression around 100 m wide within the resistant R2 basement.
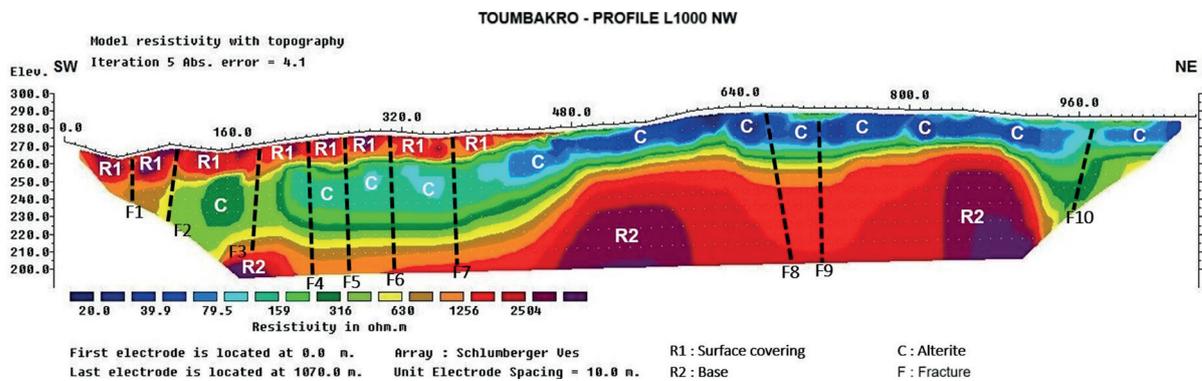

Fig. 8. *2D resistivity section of the L1000 NW profile*

Correlation of 2D resistivity sections

The juxtaposition of Toumbakro's 2D electrical resistivity sections enables us to better appreciate the continuity, as well as the lateral and vertical extension of the various layers and geoelectric structures (Fig. 9). The three geoelectric units (resistant surface cover, conductive alterite or horizon, and highly resistant sound bedrock) are clearly defined in each section. The resistivity ranges and lithological correlations of these geoelectrical units are summarized in Table 1.

At the top, the resistant surface cover, corresponding to the cuirass, has a variable geometry.

Its thickness varies between 0 m and 20 m. However, this outcropping tends to taper off towards the northeast (Fig. 9). The leading cause of this phenomenon is erosion, which is much more active in the northeastern sector than in the southwestern part.

Below the armorstone, the conductive alterite extends. The latter spread out in bench form, is relatively less conductive to the southwest than to the northeast. This contrast is linked to the erosion of the armor shell in the northeastern sector, which has subsequently favored the infiltration and accumulation of water within the underlying alteritic layer in this part of the site.

Table 1
Resistivity ranges and lithological correlations of the surveyed formations

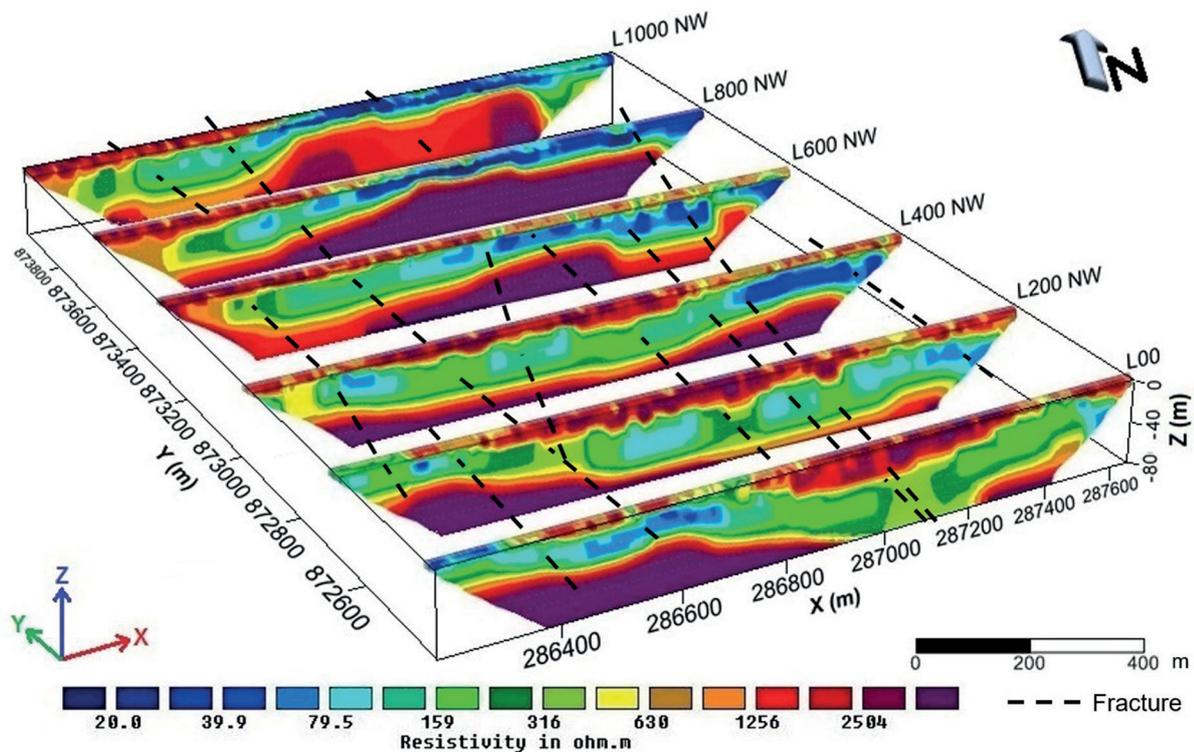| Layer	Geoelectrical unit		Resistivity range [Ω·m]	Lithology	Hydrogeological conditions
Top	R1		630–3,233	lateritic duricrust	dry and impermeable
Middle	C		20–630	alterite	moist and permeable
Base	R2	upper part	630–1,800	cracked horizon	fractured and permeable
		lower part	>1,800	sound crystalline basement	compact and impermeable

Fig. 9. *Juxtaposed 2D sections of resistivity at Toumbakro*

At the base is a basement with an irregular roof, whose depth generally decreases slightly towards the southwest. This basement approach towards the surface is again linked to erosion. From a lithological point of view, the Toumbakro basement is granitic, according to borehole data. Moreover, the transition between the alterite and the sound basement is not abrupt. Instead, it is provided by a zone of intermediate conductivity, characterized by resistivities ranging from 630 Ω·m to 1,800 Ω·m. This zone corresponds to the fissured horizon of the basement, which acts as a drainage system for the aquifers.

From a structural point of view, there is good continuity between the fractures detected on the different sections. The most important are oriented NW–SE, NNW–SSE, and N–S.

Thickness maps of layers R1 and C

In order to assess the spatial variability of the thicknesses of the superficial cover and the alterite, which play key roles in the recharge of basement aquifers, thickness maps of layers R1 and C were produced.

Layer R1

The analysis of Figure 10, illustrating the spatial distribution of the thickness of layer R1, shows that the superficial cover is irregularly distributed over the site. Indeed, as shown by sections L00, L00 NW, L800 NW, and L1000 NW, the superficial cover R1 is absent in the northern and southern parts of the Toumbakro site, thus favoring the infiltration of rainwater in these areas.
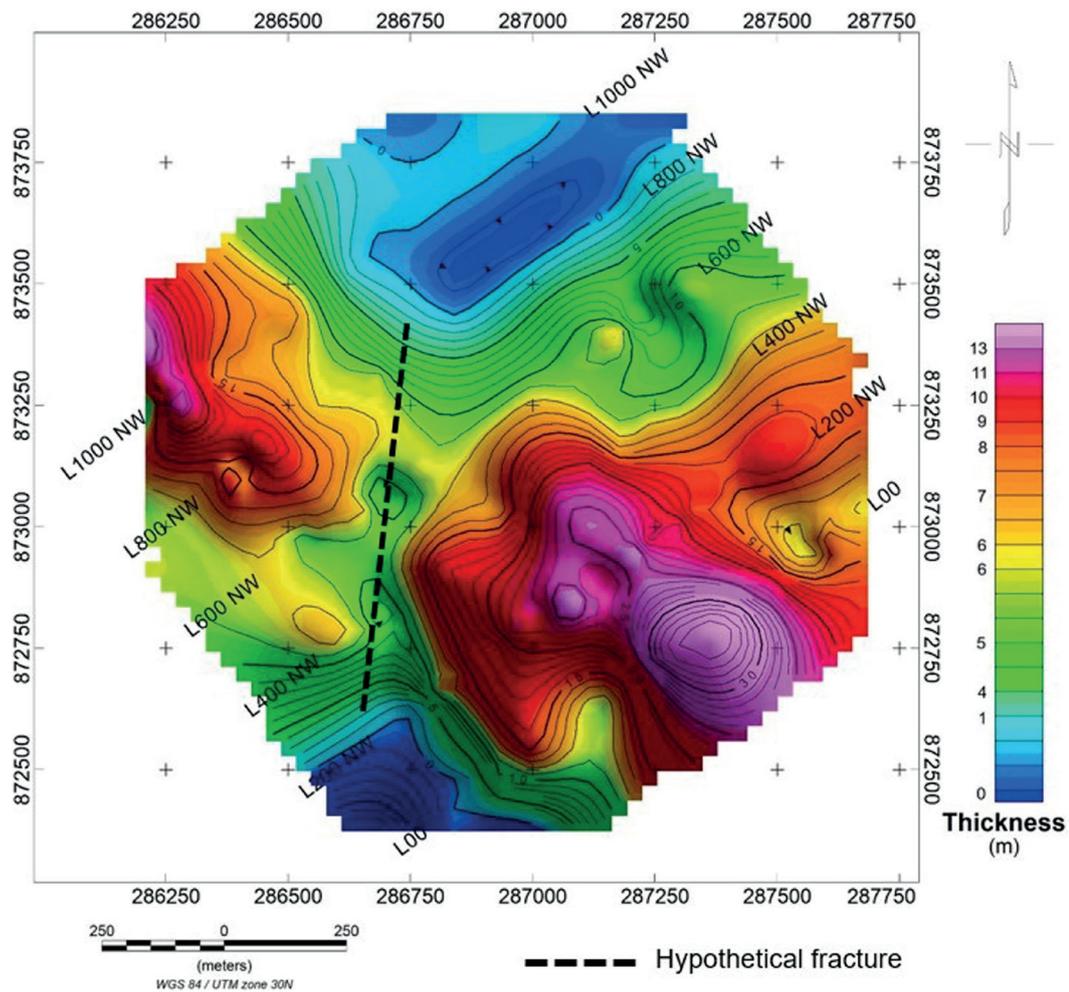

Fig. 10. *Thickness map of the R1 layer of the Toumbakro site*

On the other hand, the robustness of layer R1 is clearly observable in the eastern and western sectors of the site, with a significant decrease in its thickness in the central part. This decrease in the superficial cover thickness may be due to the combined action of the N–S oriented fracture which favored erosion. This weakened area of the iron crust, known to be dry and impermeable, will therefore serve as a drain for the infiltration of rainwater. In addition, the fracture is directly connected to areas devoid of iron crust. Consequently, the recharge of the underlying layer is clearly ensured by the areas devoid of iron crust via the fracture.

Layer C

The thickness map of layer C, corresponding to the alterites, is presented in Figure 11. The analysis of this map shows that the thicknesses of alterites at the Toumbakro site are irregular, ranging from 5 m to 40 m. However, the general trend is that the thicknesses of alterites are high below the areas covered with laterite crust, as in the eastern and western sectors. Large thickness is explained by the protective function of the laterite crust against erosion. This configuration favors hydrological conditions, reinforcing the processes of chemical weathering at depth.
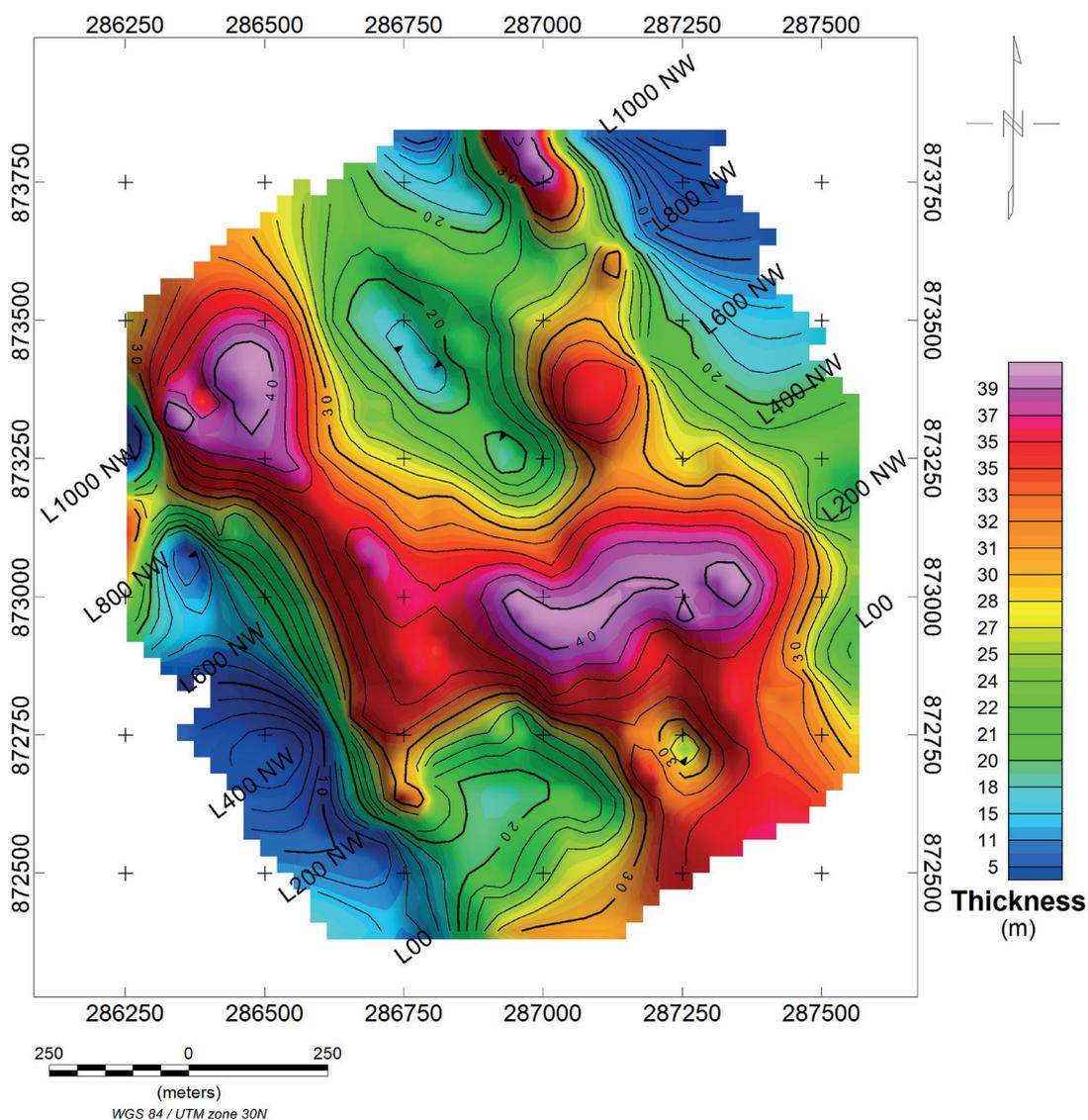

Fig. 11. Thickness map of the C layer of the Toumbakro site

Resistivity maps by level

Level 2

Figure 12 presents the apparent resistivity map of level 2, the depth of investigation of which is estimated at 10 m. Conductive formations are encountered in the north and south of the prospect. With regular contours, the conductive anomalies constitute the most humid zones of the alterites. This humidity is due to the presence of numerous pores in the first meters of the subsoil, which are fed when it rains. These are therefore superficial aquifer zones that are most often captured by traditional wells.

The rest of the prospect is mainly occupied by a resistant formation that extends along the NW–SE diagonal of the site. With more or less regular contours, the resistant anomalies are affected by several NNE–SSW oriented faults.

These superficial structures play a primary role in the recharge of the deep aquifer. Some are deeply rooted, while others are not.

Level 7

The resistivity map for level 7 reveals pronounced subsurface heterogeneity, reflecting the variability of resistivity values measured at approximately 25 m depth. At this depth, corresponding to the boundary between the weathered layer (alterite) and the fractured horizon of the bedrock, both resistive anomalies (400–1,700 Ω·m) and conductive anomalies (80–140 Ω·m) are distributed in a contrasting pattern (Fig. 13).
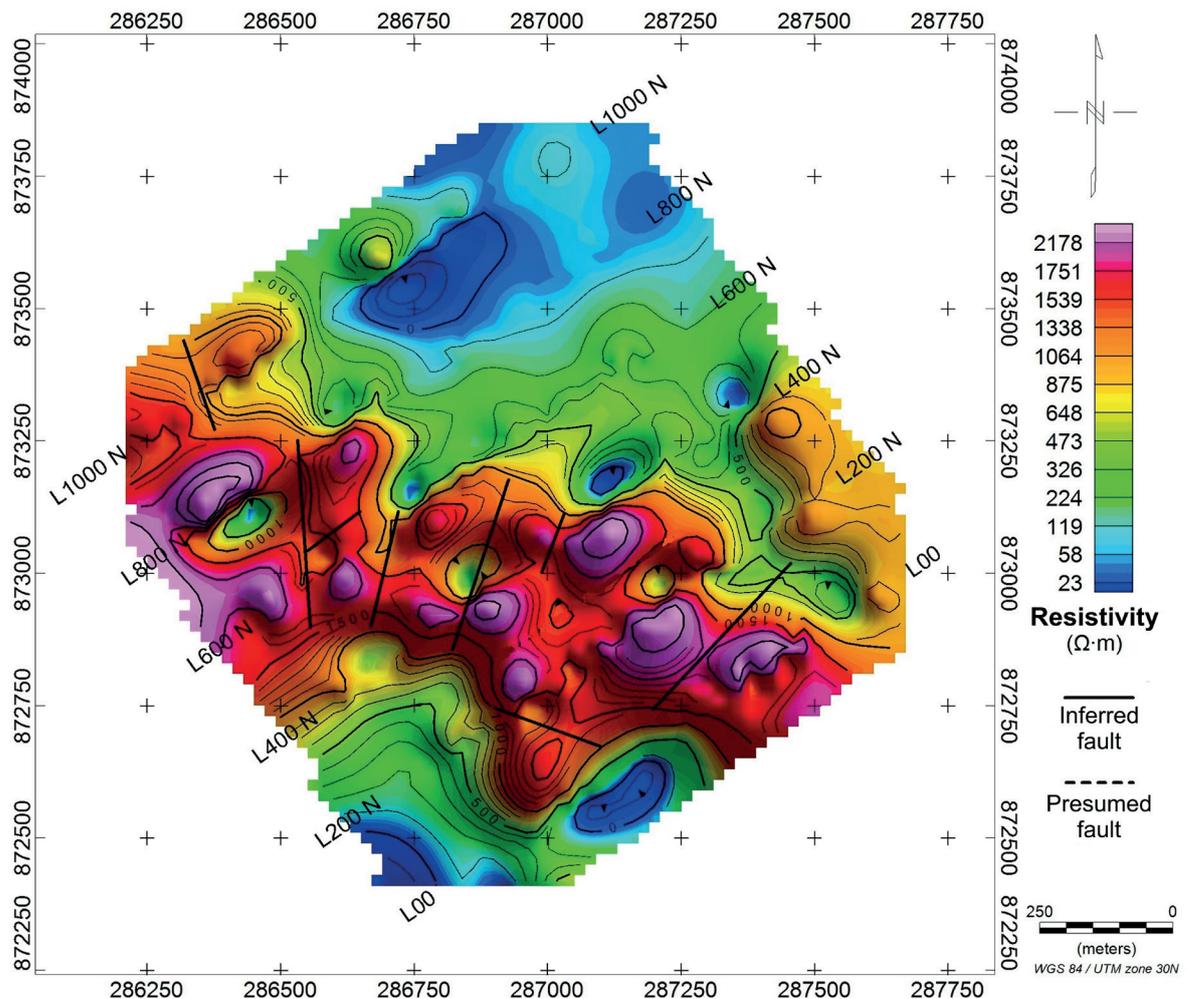

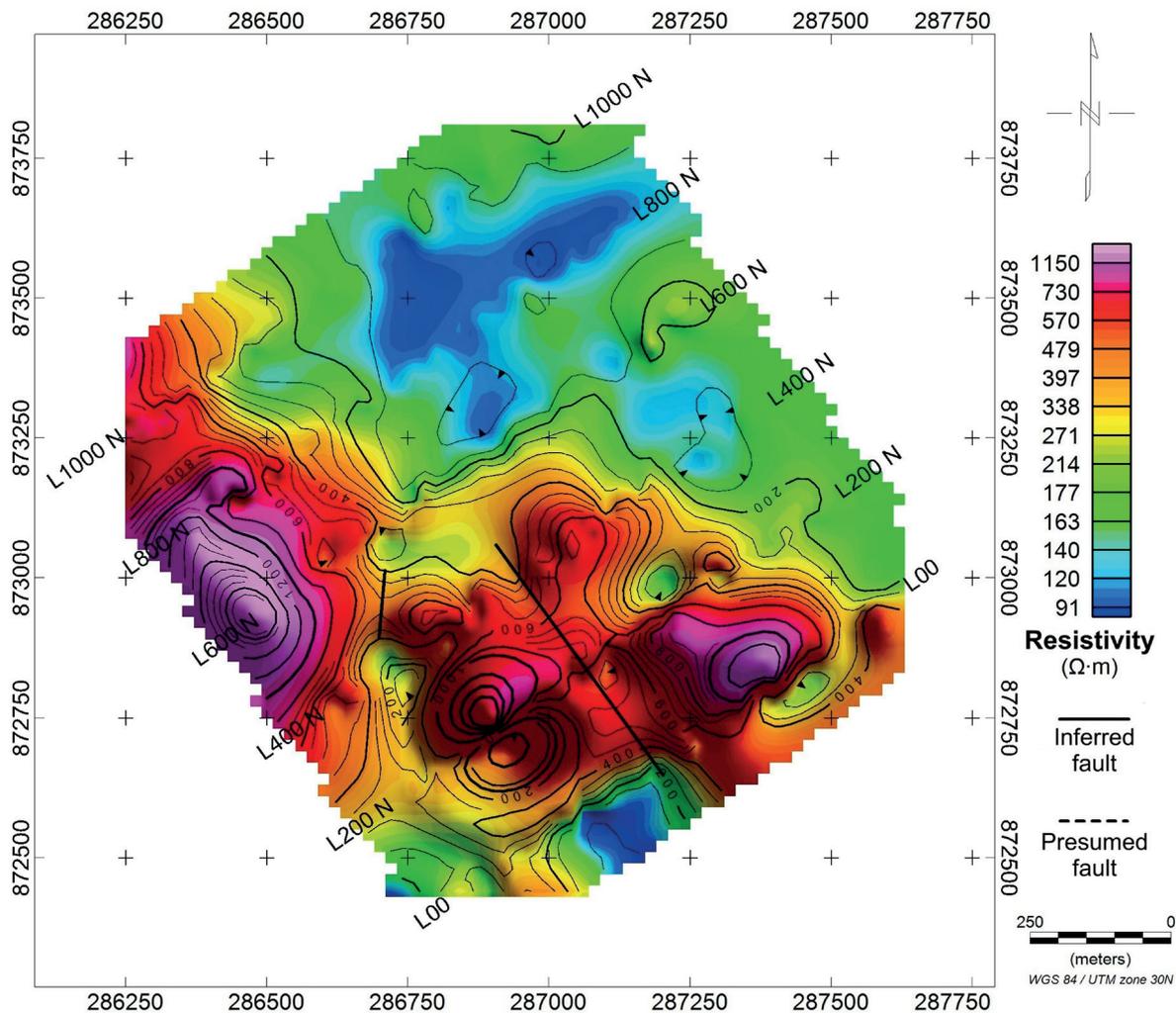**Fig. 12.** *Resistivity map of level 2*

Fig. 13. *Resistivity map of level 7*

The conductive features located toward the north and the south represent downward continuations of surface-observed conductive zones, although their shapes become increasingly irregular with depth. At the same time, a large resistive anomaly occupies the southern, northwestern, southeastern and central sectors of the site; distortions in its geometry reveal faulting with orientations N–S, NW–SE, and NE–SW. These faults appear to be superficial since they do not extend downward beyond the mapped resistive body.

The transition from resistive to conductive domains is gradual, delineated by an intermediate zone with resistivity values between $160\,\Omega\cdot m$ and $330\,\Omega\cdot m$.

Level 12

The apparent resistivity map for level 12 reveals both conductive and resistive structures, beyond level 7, with resistivity ranging from $200\,\Omega\cdot m$ to $970\,\Omega\cdot m$, corresponding to depths deeper than 45 m, which suggests the presence of the bedrock at that depth. Low resistivity values ($200–260\,\Omega\cdot m$) are attributed to conductive structures, while high resistivity values ($420–970\,\Omega\cdot m$) correspond to resistive structures; intermediate structures show resistivities between $260\,\Omega\cdot m$ and $420\,\Omega\cdot m$ (Fig. 14).

As observed in previous levels, the resistive structure is located in the northwest, southeast, south and central parts of the site, with a broad, irregularly shaped resistive anomaly lacking a marked orientation.
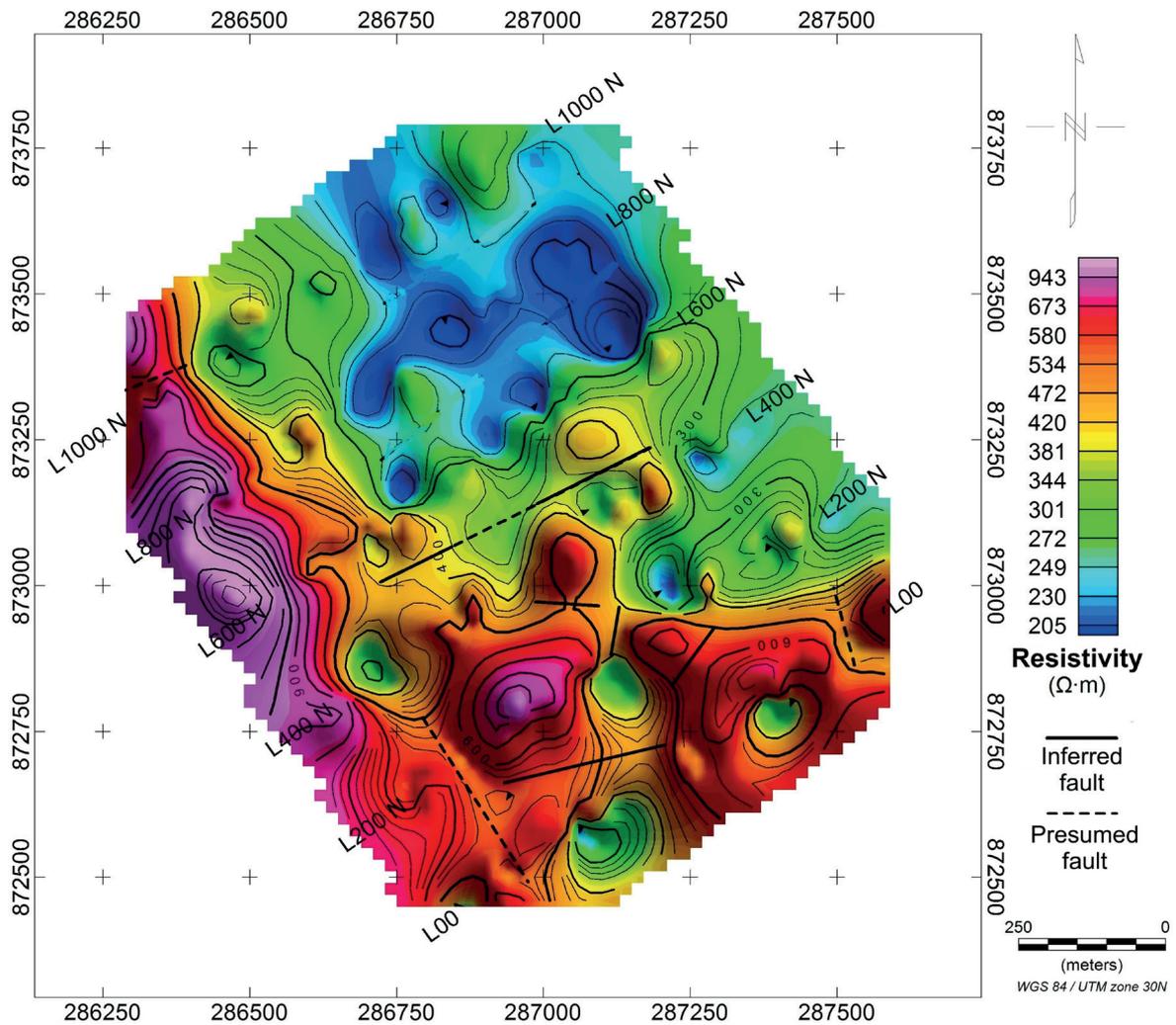
Fig. 14. *Resistivity map of level 12*

The conductive structures are located exclusively in the north of the site, in contrast with the previous maps where they were also present in the south. The deep conductive anomalies have oval-shaped contours and distortions, associated with faults oriented NE–SW, while other faults within the resistive domain show varying orientations (NNE–SSW, NNW–SSE, E–W and N–S).

Intermediate structures, with resistivities ranging from 260 Ω·m to 420 Ω·m, stand out between the conductive and resistive zones. The most significant intermediate structure is located to the east, characterized by irregular contours and an extension toward the northwest, indicating transitional phases between the conductive and resistive domains.

3D conceptual aquifer model

Interpreting the Toumbakro resistivity sections has produced a 3D geological model (Fig. 15). This model highlights four layers:
- the lateritic duricrust;
- the alterite;
- the cracked horizon;
- sound crystalline basement.

Therefore, the three layers described by the classic conceptual model in the basement zone are present: the saprolite represented by the lateritic duricrust and the alterite, the fissured horizon, and the sound basement.

The geological model thus described explains the hydrogeological behavior of the Toumbakro

aquifer system. The presence of the armorstone on the ridges favors meteoric runoff towards low-lying areas, which become the preferred recharge zones. Here, runoff is concentrated and infiltrates through the porous, permeable alterite.

In addition, the geological model for Toumbakro shows a depression in the sound basement to the east of the site. This depression may be linked to the play of a fracture that dragged this compartment of the basement lower. This zone is likely to be a potentially hydric zone.

In the context of basement aquifers in humid tropical environments, understanding the vertical organization of the reservoir is essential for characterizing local hydraulic potential. In this regard, particular attention is given to the fractured basement horizon, which constitutes the main transmissive level of the aquifer system. This horizon, predominantly intercepted by boreholes, exhibits an average thickness of approximately 10 m, with a maximum value reaching 48 m (Fig. 16).
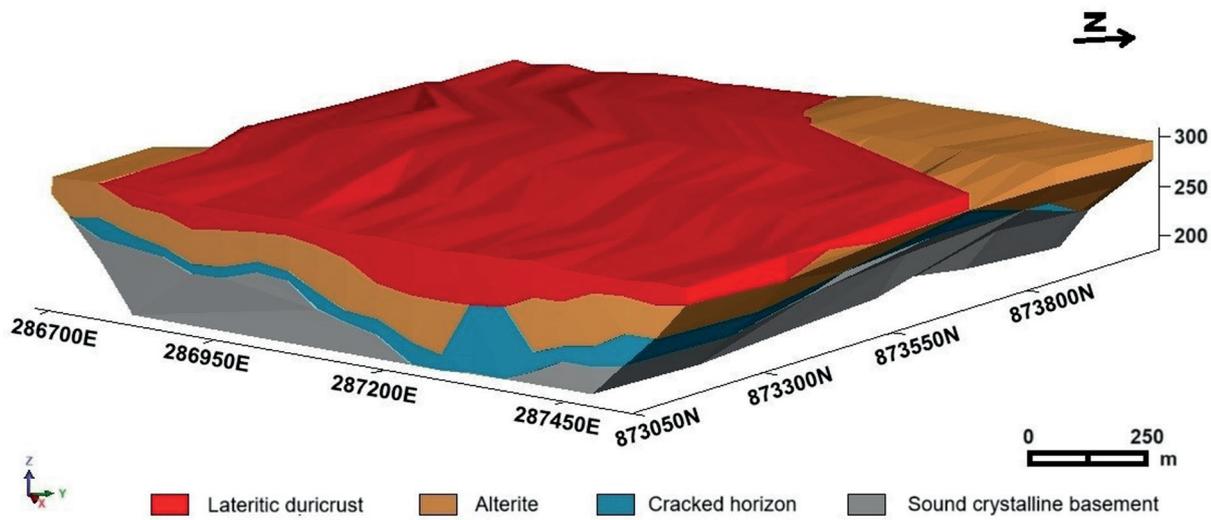

Fig. 15. *3D conceptual model of the Toumbakro aquifers*
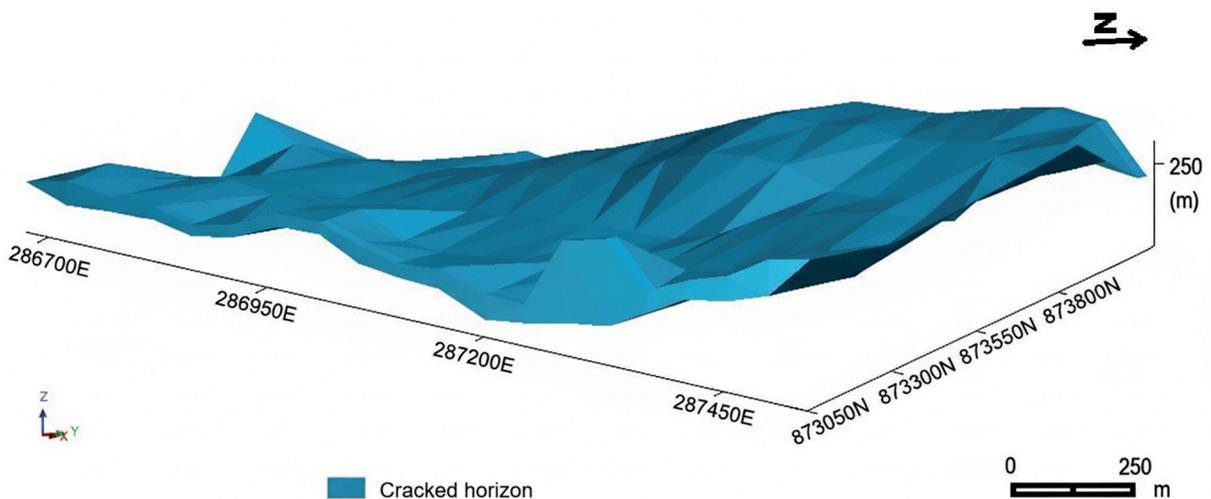

Fig. 16. *3D conceptual model of the cracked horizon, Toumbakro*

The morphological variability of the basement topography results in an irregular geometry that promotes the gravitational drainage of water stored in the overlying weathered horizons toward the fractured zones. These fractures play a key role by ensuring both the circulation and dynamic storage of groundwater within the weathered basement.

DISCUSSION

Electrical imagery is used to characterize the Toumbakro aquifer system, which is vertically structured from top to bottom with three distinct layers:

– alterite, which can be divided into two sub-layers (alloterite and isalerite) corresponding to surface covering;
– fractured rock corresponding to conductive zone;
– sound rock corresponding to resistant bedrock.

This structuring is similar to that described by Wyns et al. (2004), Dewandel et al. (2006), Courtois et al. (2009), Lachassagne et al. (2011), Koïta et al. (2013), Langman et al. (2015), and Soro (2017). For these authors, the hydraulic conductivity of basement aquifers is due to the weathering process and not to tectonics and lithostatic decompression. Alteration, therefore, plays a major role in groundwater recharge.

Although several authors have described the supposed structure of basement aquifers and reported that their fracturing is of tectonic origin (Savadogo et al. 1997, Razack & Lasm 2006), they have not proved it. Tectonics cannot be invoked as a genetic concept explaining the origin of cracks and/or secondary fractures in rocks (Lachassagne et al. 2011). According to the latter, a fracture is a complex, ancient, and profound structure in tectonically stable zones like most of the world's basement zones. Strictly speaking, fractures are located several kilometers underground and cannot be captured by geophysical investigations or standard boreholes, whose standard depths are around one hundred meters. Consequently, hydraulic installations guided by the characterization of aquifer geometry and structure must also necessarily consider alterites.

Compared with that proposed by Koïta et al. (2013) for Côte d'Ivoire and Soro (2017) for Burkina Faso, the weathering profile from this study reveals

similarities and differences in geometry and structure. The geological formations studied at Bouaké (Côte d'Ivoire) and Sanon (Burkina Faso) underwent the same geological events during the Eburnian orogenic cycle dated between 2,400 Ma and 1,600 Ma (Thiéblemont et al. 2004, Lompo 2010).

The geological profile of Toumbakro shows a superposition of three layers, identical to that proposed by Koïta et al. (2013) and Soro (2017): alterite, fissured horizon, and sound rock. Moreover, at Toumbakro, weathering thickness is higher, whereas cuirasses are abundant but low above granite. This configuration is in contrast to that observed in Burkina Faso, where alterite thickness is low at the level of the cuirassed buttes (towards the ridges) but high in the valley (Soro 2017).

In humid environments like Côte d'Ivoire, cuirasses are often dislocated (a few residual blocks remain) or completely dismantled following subsidence of the underlying ground and a wetter climatic phase (Avenard et al. 1971).

Nevertheless, in the Sudano-Sahelian environment, armor-covered ridges appear as extensive, compact blocks that have resisted dismantling. Thus, the occupation of the ridges by the dislocated cuirass at Toumbakro does not favor runoff to the detriment of the infiltration which takes place. In turn, this favors the alteration of the bedrock and, above all, recharge of the underground water table.

CONCLUSION

The electrical resistivity tomography at Toumbakro enabled us to delineate the various layers and identify the preferential groundwater recharge zones. Three main layers were identified: the sometimes non-existent cuirass and an alterite layer representing the superficial cover, the fissured horizon, and the sound basement. The fractures detected run in NW–SE, NNW–SSE, and N–S directions. These results, coupled with lithological data, were used to build a 3D conceptual model showing the organization of geological formations and the structure of aquifers in this part of central Côte d'Ivoire.

These results provide a fundamental basis for a comprehensive understanding of the hydrogeological potential of the region. Further investigations could include reconnaissance boreholes

aimed at validating *in situ* the lithological nature of the formations, as well as the continuity and permeability of the identified fractured structures. In addition, the integration of other geophysical methods, such as magnetometry or gravimetry, together with hydrochemical analyses, would contribute to refining hydrogeological models and optimizing strategies for the sustainable exploitation and management of water resources.

REFERENCES

Assemian A.E., Soro D. & Soro N., 2023. Caractérisation morphologique du paysage du département de Bouaké, Centre de la Côte d'Ivoire. *Geotrop*, 1, 5–20.

Avenard J.M., Eldin M., Girard G., Sircoulon J., Touchebeuf P., Guillaumet J.L. & Adjanohoun E., 1971. *Le milieu naturel de Côte d'Ivoire*. Mémoire, 50, ORSTOM, France.

Courtois N., Lachassagne P., Wyns R., Blanchin R., Bougaïré F.D., Somé S. & Tapsoba A., 2009. Large scale mapping of hard rock aquifer properties applied to Burkina Faso. *Ground Water*, 48(2), 269–283. https://doi.org/10.1111/j.1745-6584.2009.00620.x.

Dewandel B., Lachassagne P., Wyns R., Marechal J.C. & Krishnamurthy N.S., 2006. A generalized 3D geological and hydrogeological conceptual model of granite aquifers controlled by single or multiphase weathering. *Journal of Hydrology*, 330(1–2), 260–284. https://doi.org/10.1016/j.jhydrol.2006.03.026.

Dewandel B., Perrin J., Ahmed M.S., Aulong S., Hrkal Z., Lachassagne P., Samad M. & Massuel S., 2010. Development of a tool for managing groundwater resources in semi-arid hard rock regions: application to a rural watershed in South India. *Hydrological Processes*, 24(19), 2784–2797. https://doi.org/10.1002/hyp.7696.

Günther T., 2004. *Inversion methods and resolution analysis for the 2D/3D reconstruction of resistivity structures from DC measurements*. University of Mining and Technology, Freiberg [Ph.D. thesis].

Koïta M., Jourde H., Koffi K.J.P., Silveira K.S.D. & Biaou A., 2013. Characterization of weathering profile in granites and volcanosedimentary rocks in West Africa under humid tropical climate conditions. Case of the Dimbokro Catchment (Ivory Coast). *Journal of Earth System Science*, 122(3), 841–854. https://doi.org/10.1007/s12040-013-0290-2.

Kouassi A.M., Kouamé K.F., Goula Bi T.A., Lasm T., Paturel J.E. & Biémi J., 2008. Influence de la variabilité climatique et de la modification de l'occupation du sol sur la relation pluie-débit à partir d'une modélisation globale du bassin versant du N'zi (Bandama) en Côte d'Ivoire. *Revue Ivoirienne des Sciences et Technologies*, 11, 207–229.

Lachassagne P., Wyns R. & Dewandel B., 2011. The fracture permeability of hard rock aquifers is due neither to tectonics, nor to unloading, but to weathering processes. *Terra Nova*, 23(3), 145–161. https://doi.org/10.1111/j.1365-3121.2011.00998.x.

Langman J.B., Blowes D.W., Sinclair S.A., Krentz A., Amos R.T., Smith L.J.D., Pham H.N., Sego D.C. & Smith L., 2015. Early evolution of weathering and sulfide depletion of a low-sulfur, granitic, waste rock in an Arctic climate: A laboratory and field site comparison. *Journal of Geochemical Exploration*, 156, 61–71. https://doi.org/10.1016/j.gexplo.2015.05.004.

Lompo M., 2010. Paleoproterozoic structural evolution of the Man-Leo Shield (West Africa). Key structures for vertical to transcurrent tectonics. *Journal of African Earth Sciences*, 58(1), 19–36. https://doi.org/10.1016/j.jafrearsci.2010.01.005.

Loukou K.G.H., Kouamé L.N. & Sombo B.C., 2022. Contribution of aeromagnetism to the lithostructural identification of the aquifer system of Bouaké department (Central Ivory Coast). *IOSR Journal of Applied Geology and Geophysics*, 10(1), 1–11.

MacDonald A.M. & Davies J., 2000. *A brief review of groundwater for rural water supply in sub-Saharan Africa*. Technical Report, WC/00/33, British Geological Survey, United Kingdom.

Razack M. & Lasm T., 2006. Geostatistical estimation of the transmissivity in a highly fractured metamorphic and crystalline aquifer (Man-Danane Region, Western Ivory Coast). *Journal of Hydrology*, 325(1–4), 164–178. https://doi.org/10.1016/j.jhydrol.2005.10.014.

Savadogo A.N., Nakolendousse S. & Diallo S., 1997. Étude comparée de l'apport des méthodes électromagnétiques MaxMin et électriques dans l'implantation des forages à gros débits dans les régions de socle cristallin du Burkina Faso. *Journal of African Earth Sciences*, 24(1–2), 169–181. https://doi.org/10.1016/S0899-5362(97)00034-1.

Soro D.D., 2017. *Caractérisation et modélisation hydrogéologique d'un aquifère en milieu de socle fracturé: Cas du site expérimental de Sanon (région du plateau central au Burkina Faso)*. Université Pierre et Marie Curie – Paris 6, Institut International d'Ingénierie de l'Eau et de l'Environnement, Paris [Ph.D. thesis].

Taylor R.G., Koussis A.D. & Tindimugaya C., 2009. Groundwater and climate in Africa – a review. *Hydrological Sciences Journal*, 54(4), 655–664. https://doi.org/10.1623/hysj.54.4.655.

Thiéblemont D., Goujou J.C., Egal E., Cocherie A., Delor C., Lafon J.M. & Fanning C.M., 2004. Archean evolution of the Leo Rise and its Eburnean reworking. *Journal of African Earth Sciences*, 39(3–5), 97–104. https://doi.org/10.1016/j.jafrearsci.2004.07.059.

Wyns R., Baltassat J.M., Lachassagne P., Legchenko A., Vairon J. & Mathieu F., 2004. Application of proton magnetic resonance soundings to groundwater reserve mapping in weathered basement rocks (Brittany, France). *Bulletin de la Société Géologique de France*, 175(1), 21–34. https://doi.org/10.2113/175.1.21.